Satellite-supported flood forecasting in river networks: a real case study

Javier García-Pintado[a,b,], David C. Mason[c], Sarah L. Dance[a,b], Hannah L. Cloke[a,c], Jeff C. Neal[d], Jim Freer[d], Paul D. Bates[d]

[a]School of Mathematical and Physical Sciences, University of Reading, UK
[b]National Centre for Earth Observation, University of Reading, Reading, UK
[c]School of Archaelogy, Geography and Environmental Science, University of Reading, UK
[d]School of Geographical Sciences, University of Bristol, Bristol, UK

Abstract

Satellite-based (e.g., Synthetic Aperture Radar [SAR]) water level observations (WLOs) of the floodplain can be sequentially assimilated into a hydrodynamic model to decrease forecast uncertainty. This has the potential to keep the forecast on track, so providing an Earth Observation

1. Introduction

While there are recent advances in low-cost telemetered networks for long-life flood monitoring and warning applications, oriented to be deployed over large areas (e.g., Marín-Pérez et al., 2012), the actual number of operational gauges is actually declining in the world (Vörösmarty et al., 2001 horizontal channel with a bump, with known in ow and known downstream slope. Later, Durand et al. (2014

2. Methods

2.1. Study domain

This study focuses on an area of the lower Severn and Avon rivers in the South West United Kingdom, over a 30.6×49.8 km^2 (1 524 km^2) domain. Fig. 1 depicts the study area for the flood model. Four our investigation, we used a real case based on an event that occurred in November 2012. We used a previous event in July 2007 in the same location as a calibration scenario. In the calibration event, the two major rivers suffered a substantial degree of overbank flooding. The event of 23 November–4 December 2012 recorded a maximum water depth of 5.21 m at the Saxon's Lode gauge near Tewkesbury. Also both the Severn and Avon were in flood in this event. Tewkesbury lies at the confluence of the Severn, flowing from the Northwest, and the Avon, flowing from the Northeast.

2.2. Rainfall-runoff model and inflow generation

In the experimental setup we emulated a real forecast scenario, in which the precipitation the sequence was acquired just before the flood peak in the Severn (see Fig. 3). Although the river went back in bank on 30 November, we continued the imaging as a substantial amount of water remained on the floodplain. It is worth noting that water levels on the flood plain at the end of the event were much higher than those in the channel. All CSK images were HH polarisation, providing good discrimination between flooded and non-flooded regions. Details of the overpasses are given in Table 1.

Processing level was 1C-GEC, which meant that the images were geo-corrected to 100 m. It was necessary to register the images to British National Grid coordinates using ground control points and a digital map, when a registration accuracy of better than 2 pixels (of size 2.5 m) was obtained.

Detection of the flood extent in each image was performed using the segmentation technique described in Mason et al. (2012a), which groups the very large numbers of pixels in the scene into homogeneous regions. As there was no flooding of urban areas, only the rural flood detection algorithm was used. The scale parameters for the segmentation were the same as those used in Mason et al. (2012a). A critical step is the automatic determination of a threshold on the region mean SAR backscatter, such that regions having mean backscatter below the threshold are classified as flooded, and others as un-flooded. The initial rural flood classification may be improved in a number of ways. For example, in the clean-up stage, flood regions were deleted if their mean height was above 14 m above ordnance datum (AOD). Heights were obtained from an image constructed from 24 22 km UK Environment Agency (EA) LiDAR tiles covering the hydrodynamic model domain (Fig. 1). Fig. 2 shows the flood extents detected in the images, overlain on the SAR data in the hydrodynamic model domain. The sequence shows the flood wave moving down the river, and the flood at Tewkesbury gradually dying away, starting on the Avon. In general terms, regarding the spatial coverage of the images, the Severn was imaged up to the Latitude of Worcester, the Teme up to the Longitude of Bransford, and the Avon up to the Longitude of Besford Bridge. Also, the first image (2012-11-27) just covered up to 2 km downstream from Kempsey.

WLOs were extracted from the flood extent waterlines by intersecting the extents with high resolution floodplain topography (airborne LiDAR of 1 m or 2 m pixel size) using the method described in Mason et al. (2012b). The method selects candidate waterline points in flooded rural areas having low slope and vegetation, so that small errors in waterline position have little effect on waterline level. The waterline levels and positions are corrected for the effects of double

Table 1: Details of COSMO-SkyMed overpasses.

Timestamp (UTC)	Pass	Indicence angle
27/11/12 19:20	Descending	49
28/11/12 18:01	Descending	51
29/11/12 18:20	Descending	32

2.6. The ensemble filter

We conducted synchronous assimilation of the observations. That is, the flood model simulations were sequentially interrupted as assimilation was conducted at the time of the corresponding CSK overpasses. Whenever we simultaneously estimated uncertain parameters or errors in inflow boundary conditions at the time of the assimilation, we did so as part of the data assimilation by using state space augmentation (Friedland, 1969). As the model state is augmented with model parameters, the assimilation scheme is able to take into account correlations between the errors in the parameters and the errors in the model variables. In data assimilation schemes using such an approach, the analysis updates an augmented state vector, $\in \Re^n$,

$$ = \begin{bmatrix} z \\ \end{bmatrix}; \tag{4}$$

where z is the n_s-dimensional model state (water levels in our case) and is a generic n-dimensional vector of parameters (including instantaneous inflow errors for the cases where these are simultaneously estimated). Thus, $n = n_s + n$.

The Ensemble Kalman Filter (EnKF), introduced by Evensen (1994), is characterised by a two step feedback loop: a prediction and an observation update. In each step, an ensemble of augmented state vectors is interpreted as a statistical sample of the forecast or analysis uncertainty, respectively. Thus if $\{ _i\}(i = 1, \ldots, m)$ is an m-member ensemble, then the ensemble mean is the n-vector defined by

$$\bar{} = \frac{1}{m}\sum_{i=1}^{m}$$

be indirect or not located at model grid points, so the p n matrix H, known as the observation operator (or “forward” operator) is required to map the state vector to the observation space. The Kalman gain,

$$K = \quad ^{f}(H \quad ^{f})^{T} \; H \quad ^{f}(H \quad ^{f})^{T} + R \quad ^{1}; \qquad (9)$$

is an n p matrix, where the superscript “T” denotes matrix transposition, and R is the p p observation error covariance matrix. This update may be thought of as a linear combination of the forecast and the observations, weighted by the uncertainty in the given model and observation data. The term $y = y \quad H \quad ^{f}$ is usually called the vector of “innovations”, indicating the di erence between the observations and the forecast; the Kalman gain, K contains the weights given to the innovations to update the system. $= \overline{\quad}^{a} \quad \overline{\quad}^{f}$, is called the vector of “increments” and is the di erence between the analysis and the forecast.

As well as updating the ensemble mean, we must also update the ensemble perturbations, giving an ensemble estimate of the analysis error covariance as

$$P^{a} = \quad ^{f} \quad KH \quad ^{f} \quad\quad ^{f} \; ^{T}: \qquad (10)$$

There are a number of possible computational implementations for updating the ensemble. In this work, we used an Ensemble Transform Kalman Filter (ETKF) in an unbiased formulation with a symmetric square-root (

a novel distance metric based on a channel network distance, which allows us to distinguish between flows in adjacent channels that may be close together in a Euclidean sense.

For floods developed around a channel network (e.g., a river network, as in this case study), one could expect the physical connectivity of flows to influence the development of the forecast error covariance. Thus a localization taking into account the along-network distance would not only be more physically meaningful than an "as-the-crow-flies"-based localization, but also should lead to an improved forecast skill. To this end, assuming that the flood is developed around a pre-existing (river/urban) network, the channel network can be vectorised and the chainage of the network used for calculating along-network distances. Let X be the set of points of interest for localization, and we denote as X^c the minimum-distance mapping of X into the channel network. With this, let us define our along-network metric for localization, $d_n(x_i; x_j)$, as

$$d_n(x_i; x_j) = \max\left\{d_e(x_i; x_j); d_s(x_i^c; x_j^c)\right\}; \tag{11}$$

where $d_e(\cdot;\cdot)$ denotes the "as-the-crow-flies" Euclidean distance, which is evaluated upon X and $d_s(\cdot;\cdot)$ is the distance evaluated along the chainage provided by the vectorised channel network, which is evaluated upon X^c. The rationale for including $d_e(\cdot;\cdot)$ in the definition of $d_n(\cdot;\cdot)$ is to provide a minimum distance threshold for nearby couple of points $(x_i; x_j)$, which might for

radius for bathymetry, to provide a minimal analysis of the in uence of the localization radius on the distributed bathymetry estimation and the general estimation process.

Regarding the parameter spatial support, friction was considered as two global parameters described by the Manning's coe

Table 2: Summary of lter con gurations for assimilation[a].

code	h			q			dsl			c			bat		
	u[b]	i[c]	l[d]	u	i	l	u	i	l	u	i	l	u	i	l
a	T	0.5	F	F	–	–	T	0.0	F	F	–	–	F	–	–
b	T	0.5	F	T	0.0	F	T	0.0	F	F	–	–	F	–	–
c	T	0.5	$d_e(20)$	F	–	–	T	0.0	$d_e(10)$	F	–	–	F	–	–
d	T	0.5	$d_e(20)$	T	0.0	$d_e(20)$	T	0.0	$d_e(10)$	F	–	–	F	–	–
e	T	0.5	$d_n(20)$	F	–	–	T	0.0	$d_n(10)$	F	–	–	F	–	–
f	T	0.5	$d_n(20)$	T	0.0	$d_n(20)$	T	0.0	$d_n(10)$	F	–	–	F	–	–
g	T	0.5	$d_n(20)$	F	–	–	T	0.0	$d_n(10)$	T	1.0	F	F	–	–
h	T	0.5	$d_n(20)$	F	–	–	T	0.0	$d_n(10)$	F	–	–	T	1.0	$d_n(10)$

In Fig. 4 the updated forecast error covariance between level at Bredon and levels elsewhere is also shown as the background for each configuration. Note that both the colour scales and the symbolic representation of $K_{i,j}$ are independent for each plot to ease visualisation. For this figure we have selected filters with inflow updating, as these tend to behave better than similar ones without inflow estimation (see Section 3.3 below). Also, we focus here on the situation pertaining to the assimilation of WLOs from the last CSK overpass, as this summarizes the cumulative feedback of the different filters along the sequential assimilation in the event.

Filter (b), the global filter, leads to sparsely distributed non-negligible $K_{i,j}$ values throughout the domain, with many distant observations influencing the updating at Bredon. Not only are there many significant gain values along the whole Severn, but also the highest value ($K_{i,j}^{max}$ = 0.023) at this last overpass ($t = 7$) is in a tributary of the Severn, a significant distance away from Bredon. Also, the gain values have a skewed distribution with a just a few WLOs having high gain values and then many other observations gathering around low, albeit non-negligible, values. In general, the situation is far from what one would expect from a properly constructed assimilation system, and it is also likely to hamper the robustness of the filter to possible anomalous (outlying) innovations. This situation arises from the assimilation sequence throughout the event, in which spurious correlations are not properly damped. Thus the global filter ends up with a system in which these spurious correlations have a dominant effect, leading to relationships which are unlikely to happen in the real physical system. Moreover, at this stage in the event the water levels at observation locations surrounding Bredon have a negative correlation with the level at Bredon, leading to negative gain values (red squares), which do not have any physical reason to happen. A strongly-related problem is the collapse of the variance, as the development of spurious correlations leads in turn to too much weight being put onto the observations in the early stages of the event and promotes variance collapse. As the assimilation proceeds, the global filter leads to a general underestimation of the variance and filter divergence, here exemplified via the over-flattened map of the forecast error covariance with Bredon, and its low sum of absolute values of the corresponding Kalman gain values ($\sum_{j=1}^{p}|K_{i,j}| = 0.3$).

On the other hand, filter (d), with d_e

approach.

The influence of simultaneous parameter estimation is discussed in Section 3.4. However, we include filter (l), which is similar to (f) but with simultaneous estimation of global channel friction and distributed bathymetry, to summarize that it leads to a situation which seems even more physically sound than that from (f) from the point of view of the spatial distribution and share of the Kalman gain values. The higher gain values are now very well distributed around Bredon, and with slightly higher weights given to those WLOs downstream from Bredon. The situation seems very close to ideal, with properly developed forecast error covariances, with respect to what one could expect at this stage of the event. There are a few distant minor negative gain values in the row, but given their relative values these become insignificant in the updating. Other aspects of the case are discussed in Section 3.4.

3.3. Inflow estimation

As indicated in Section 2.4, the satellite sequence was not covering the boundary condition locations for the major inflows to the flood model domain. For the three major rivers, the coverage was up to may be subject to biases because of errors or unaccounted hysteresis in the rating curves, etc.) are to the assimilation-based estimates of total inflow to the system.

Summarising Table 3, the assimilation in all filter configurations generally moves the prior inflows away from the gauged inflows. This is indicated by the positive values in parenthesis in the RMS row. As indicated, this should not be interpreted as whether the assimilation is doing a bad job. On the contrary, this may well be the case that the satellite-based WLOs are providing information, to improve the estimation of total inflows into the system, not contained either in the gauged inflow boundary condition nor in the prior inflows, forecasted from the catchment-scale hydrologic models. Without further information, to evaluate whether the assimilation is then performing well in estimating inflow errors and whether this online inflow error estimation/correction is an useful operational strategy, one needs to evaluate how the flood forecast behaves downstream and whether the estimated inflow errors are properly allocated to the corresponding sources. In the context studied, this refers to a loose relationship between flooded areas and corresponding assumed point inflow boundary conditions.

For example, Table 3 shows two opposed configurations with similar RMS [filter (b) and filter (l)]. Filter (b) is in fact the only configuration which brings the updated inflow from Bewdley closer to the gauged inflows ($\mathrm{RMSE} = -2.95\ \mathrm{m^3\,s^{-1}}$). Fig. 5 shows the evolution of the updated inflows at Bewdley for these two filters; i.e. the global filter (b), and the filter (l), with d_n-metric localization and simultaneous friction and bathymetry estimation. Filter (b) behaves rather erratically, in agreement with the discussion about the lack of robustness of the filter in Section 3.2. For example, the assimilation of the WLOs from the 2nd and 6th overpasses creates positive increments, which are interspersed with the negative increments related to the 3rd and the 7th overpasses. On the other hand, filter (l) has a small increment at the 1st overpass, and then onwards, the increments become negligible. To provide some insight into the reasons leading to these different situations, let us focus now on the forecast error covariances after the 1st assimilation step between the flows at Bewdley (inflow to the Severn) and the water levels elsewhere. This is depicted by Fig. 6 for the same filters as Fig. 4. Filter (b) shows a strong component of the updating is due to spurious correlations, not only from smaller tributaries downstream, but also even from a set of negative Kalman gain values assigned to WLOs too distant in the Avon. The evolution of the spatial distribution of the Kalman gain values in filter (b) is highly erratic along the event, with the highest gain values continually displacing from one location to another between sequential assimilation steps (not shown; available on request), and leading to a degenerate situation by the 7th overpass, where a highly skewed dsitribution of the gain values (in the row) and the growth of spurious correlation with WLOs in smaller tributaries is very similar to that of Fig. 4 for the same filter.

Filter (d), however, adequately takes into account the most upstream observations in the Severn to update the inflows. Still there are non negligible spurious gain values in tributaries downstream. Filters (f) and (l) are both similar to (d) but more effective at damping the spurious correlation with water levels at downstream tributaries. The evolution of the distribution of Kalman gain values in the sequential assimilation is then very similar for (d), (f), and (l) (not shown). For these, the spatial distribution of gain values is much more stable in time, and the filters are e without/with simultaneous inflow estimation indicates that the online inflow updating lead to improved forecasts if localization is applied [e.g., (c) versus (d), or (e) versus (f)]. This improvement also applies if friction is simultaneously estimated [(g) vs. (j)], but the statistics are similar for those configurations with simultaneous bathymetry estimation [(h) vs. (k), or (i) vs. (l)].

On the other hand, in the global filters [(a) vs. (b)] the simultaneous inflow updating further promotes ensemble collapse and divergence. This is reflected in the larger RMSE in (b) with respect to (a), and can be seen, e.g., in the water level time series plots for configuration (b) in Worcester in the Severn (Fig. 7), Mythe Bridge downstream in the Severn close to the junction with the Avon (Fig. 8), or Bredon in the Avon (Fig. 9). Thus, just the filters with localization, with improved accounting of the forecast error covariances, are able to better exploit the added freedom of inflow updating, behaving better throughout the event than the versions with prescribed inflows. The benefit of the simultaneous inflows estimation shown in Table 4 is also shown by a pairwise comparion of the filter with d_e-metric localization [(c) vs. (d)] or the filters with d_n-metric localization [(e) vs. (f)] in time series (Figs. 7, 8, and 9).

Table 3: RMSE of inflows for filters with inflow updating.[a,b]

	b	d	f	j	k	l
besford_bridge_q	1.84(0.24)	1.94(0.35)	1.79(0.20)	1.74(0.15)	1.82(0.23)	1.75(0.16)
bewdley_q	82.87(-2.95)	122.26(36.44)	108.86(23.04)	107.34(21.52)	97.63(11.81)	95.92(10.10)
evesham_q	33.43(12.79)	32.07(11.43)	23.82(3.18)	23.49(2.85)	23.62(2.98)	23.93(3.30)
harford_hill_q	1.12(0.37)	0.96(0.20)	1.32(0.57)	1.21(0.46)	0.96(0.20)	0.95(0.19)
hinton_q	0.65(0.10)	0.48(-0.07)	0.49(-0.06)	0.49(-0.06)	0.53(-0.02)	0.52(-0.03)
kidder_callows_ln_us_q	1.24(-0.60)	1.20(-0.64)	1.42(-0.42)	1.41(-0.42)	1.50(-0.33)	1.54(-0.30)
knightsford_bridge_q	48.38(4.66)	49.56(5.84)	59.34(15.61)	58.08(14.35)	51.13(7.41)	49.00(5.27)
RMS[c]	38.42(5.27)	51.33(14.61)	47.73(10.59)	46.99(9.84)	42.61(5.39)	41.72(4.49)

[a] [$m^3 s^{-1}$]. RMSE measured against gauged inflows within [2012-11-27 19:20:00 UTC, 2012-12-05 23:00:00 UTC].
[b] In parentheses is the RMSE minus the RMSE of the prior inflows (forecast of the hydrologic models).
[c] RMS of the values for the corresponding column.

Table 4: RMSE of water levels at gauged locations for the filters evaluated.[a]

	a	b	c	d	e	f	g	h	i	j	k	l	m
bransford_h	0.79	0.90	0.80	0.95	0.81	1.34	0.85	1.00	0.98	1.30	1.14	1.18	1.00
bredon_h	0.66	0.65	0.69	0.40	0.69	0.40	0.67	0.85	0.89	0.45	0.74	0.72	0.60
kempsey_h	1.22	1.43	1.26	0.57	1.27	0.60	1.17	1.22	1.28	0.65	1.16	1.18	1.06
mythe_bridge_h	0.69	0.79	0.73	0.50	0.73	0.46	0.72	0.86	0.79	0.51	0.76	0.76	0.65
saxons_lode_us_h	0.94	1.12	0.98	0.56	0.99	0.55	0.94	1.16	1.22	0.60	1.20	1.26	1.24
shuthonger_h	0.38	0.49	0.42	0.22	0.42	0.22	0.41	0.63	0.55	0.25	0.52	0.55	0.39
worcester_h	1.33	1.55	1.37	0.48	1.38	0.61	1.28	1.29	1.48	0.66	1.27	1.23	1.02
RMS	0.91	1.06	0.94	0.56	0.95	0.68	0.91	1.03	1.07	0.70	1.01	1.02	0.90

[a] [m]. RMSE measured against gauged water levels within [2012-11-27 19:20:00 UTC, 2012-12-05 23:00:00 UTC].

Overall, the two filters with better performance in the group without friction and/or bathymetry estimation (a–f) are the filters with localization and simultaneous inflow estimation. According to Table 4, these are filter (d) with d_e-metric localization (RMS = 0.56 m), and (f) with d_n-metric localization (RMS = 0.68 m). While the RMS is slightly better for filter (d), the evaluation of the forecast error covariance (for example, as shown in Figs. 4, and 6) indicates that the along-network-based localization is preferable as a forecast error covariance moderation process, and helps further to prevent the development of spurious correlations, which should be adequate for local parameter estimation. Also in the downstream areas, where most of the flood occurred (Mythe Bridge, Saxons Lode US, and Bredon) the RMSE is equal or better for filter (f).

Thus in the following section on simultaneous parameter estimation we focus the discussion on filter configurations with d_n-based localization.

3.4. Parameter estimation

In this section we focus on filter configurations with simultaneous friction and/or bathymetry be reflected in a sensitivity of the flood forecast to the (likely) improved friction estimates, so leading to a better forecast. However, the convergence being gradual, it seems the DA-forecast cycle does not have time to benefit from the updated friction.

Fig. 11 shows the evolution of bathymetry, along the event, for the rivers Severn and Avon, and filter configuration (k). The chainage 0 for the Avon refers to its junction with the Severn, very close to Mythe Bridge. All the filters including bathymetry estimation with identical localization radius for bathymetry, either with/without simultaneous friction estimation, or with/without simultaneous inflow bias correction (i.e. filters [h], [i], [k], and [l]) show a nearly identical convergence, supporting the robustness of the estimation shown in Fig. 11, independently from other factors. The sequential updating converges systematically toward a profile in which, after the event, the lower part of the Severn is nearly 2 m higher than the prior bathymetry, and the transect between Saxons Lode US and Kempsey gauges is lower than the prior (at some points reaching 1.5 m of difference with respect to the prior). The highest increments in the updating are due to the assimilation of WLOs from the first overpass. Thereafter, the updating increments become gradually smaller along time. The updatings summarize the influence of the channel conveyance on the flood development. Globally, the SAR-WLOs seem to indicate that the prior bathymetry was leading to a model which overestimated the release of water from the flooded domain during the early stages of the event. The sequential increments in the bathymetry along the Avon are also systematic, leading to a raised channel bed profile with respect to the prior. In both rivers, the effect of the localization is clearly visible. That is, moving upstream, the increments become gradually smaller as the bed locations move away from the observations (e.g., in the Severn the WLOs roughly generally covered up to the 40 km chainage coordinate, close to Kemspey). The consistent and systematic sequential increments indicate a physical basis for these, as happened with

5 km of the domain remained unobserved during the event (i.e., as a results of the multicriteria screening to obtain the WLOs to be assimilated, none of these was located in the last 5 km of the Severn within the domain). As in the experimental design we did not provide any inflation for bathymetry, the channel bed estimated variance is gradually reduced along the sequential assimilation, and by time the most downstream area (around Mythe Bridge and toward the South) has the strongest influence on the release of water from the domain, the bathymetry spread is too low to be properly updated (and the WLOs did not reach the last 5 km of the South of the domain —see, e.g., Fig. 4—). A plot similar to Fig. 11, but regarding the evolution of the bathymetry ensemble spread along the sequential assimilation indicates that the standard deviation of bathymetry around Mythe Bridge decreases from an initial 0.8 m until a final 0.4 m (not shown; available on request). The chosen $= 0.15$ in the bathymetry error generation, reflects our confidence in the prior bathymetry estimates.

Overall, it seems that either the chosen 5 000 m spatial correlation length in the stochastic generation of the bathymetry error was too high or the 10 000 m localization window for the d_n-based localization for bathymetry estimation was too high (or both factors), leading to an overshooting of the downstream bathymetry increments, and subsequent problems. To test this point, we conducted a further simulation (filter configuration [m]) with 5 000 m as localization window for bathymetry estimation. In effect, the general trends in the sequential bathymetry updating are similar to the previous experiments, but the increments gradually fade downstream (see supplementary material). This translates into a steeper recession limbs (closer to those of configuration [f]) and better statistics (see [m] versus [l] in Table 4). Thus everything indicates that by tuning the localization radii and correlation length in the bathymetry error generation the simultaneous parameter/state estimation process could be further improved. However, as indicated in the experimental design, to provide a detailed exploration of the parameter space and localization parameters goes beyond the scope of the current study.

4. Conclusions

We have shown that under a relatively complex scenario with simultaneous uncertain inflows into a flooded domain, a satellite-based forecast of the flood with high accuracy is possible through the assimilation of the satellite-based WLOs into a flood forecast model. However, several aspects should be taken into account for a successful operational application of EnKF-based assimilation of EO-based WLOs and forecast. First, a moderation of the forecast error covariance based on spatial localization is necessary to avoid filter divergence. Second, inflow estimation also improves the forecast. This second point is only valid if localization is applied, otherwise the incorrect forecast error covariance development in the global filter prevents any benefit from online inflow estimation and bias correction. Third, the implementation should consider the possible uncertainty in model parameters and their simultaneous online estimation.

The study shows that if the physical connectivity of flows is considered in the form of the newly proposed along-network metric for the localization, the development of forecast error covariances is sounder than that resulting from the use of a standard as-the-crow-flies distance. The relevance of this regarding the forecast skill should depend on the geometry of the network studied case. In other cases (steeper rivers, faster flow, etc.) things might be different. The localization parameters used in the case study for bathymetry estimation seem to be far from optimal, and tuning these parameters could lead to a better estimates in the inverse problem (i.e.

References

Anderson, J. L. (2001). An ensemble adjustment kalman filter for data assimilation. *Mon. Wea. Rev.*, *129*, 2884–2903. URL: http://dx.doi.org/10.1175/1520-0493(2001)129<2884:AEAKFF>2.0.CO;2. doi:10.1175/1520-0493(2001)129<2884:AEAKFF>2.0.CO;2.

//dx.doi.org/10.1175/1520-0493(2001)129<2776:DDFOBE>2.0.CO;2 . doi:10.1175/1520-0493(2001)129$<$2776:DDFOBE$>$2.0.CO;2

Hostache, R., Lai, X., Monnier, J., & Puech, C. (2010). Assimilation of spatially distributed water levels into a shallow-water ood model. part ii: Use of a remote sensing image of mosel river. Journal of Hydrology, 390, 257–268. URL: http://www.sciencedirect.com/science/article/pii/S0022169410004166 . doi:10.1016/j.jhydrol.2010.07.003 .

Houtekamer, P. L.1(/G /et587 -99.t16.6uD(/G /etH)-287(L.1-2876(21998051.)-3476(Data-287(Lasimilation)-2580ensem Mon. 1-2876055ea.g-28rttion)-2580ensem Rev, 126, 796–811. URL: http://dx.doi.org/10.1175/1520-0493(21998051126<0796:DAUAEK>2.0.CO;2 . doi:10.1175/1520-0493(21998051126<0796:DAUAEK>2.0.CO;2

5194/hess-17-3499-2013 .

Raclot, D. (2006). Remote sensing of water levels on floodplains: a spatial approach guided by hydraulic functioning. International Journal of Remote Sensing, 27, 2553–2574. URL: http://dx.doi.org/10.1080/01431160600554397. doi:10.1080/01431160600554397.

Roux, H., & Dartus, D. (2008). Sensitivity analysis and predictive uncertainty using inundation observations for parameter estimation in open-channel inverse problem. Journal of Hydraulic Engineering, 134, 541–549. doi:10.1061/(ASCE)0733-9429(2008)134:5(541) .

Ryu, J. (2009). Application of hspf to the distributed model intercomparison project: Case study. Journal of Hydrologic Engineering, 14, 847–857. URL: http://dx.doi.org/10.1061/(ASCE)HE.1943-5584.0000054. doi:10.1061/(ASCE)HE.1943-5584.0000054. arXiv:http://dx.doi.org/10.1061/(ASCE)HE.1943-5584.0000054 .

Schultz, C., Ahmed, S., Mandel, R., & Moltz, H. (2013). Improvement in hspf's low-flow predictions by implementation of a power law groundwater storage-discharge relationship. JAWRA Journal of the American Water Resources Association, (pp. 1–19). URL: http://dx.doi.org/10.1111/jawr.12144. doi:10.1111/jawr.12144 .

Schumann, G., Hostache, R., Puech, C., Hoffmann, L., Matgen, P., Pappenberger, F., & Pfister, L. (2007). High-resolution 3-d flood information from radar imagery for flood hazard management. Geoscience and Remote Sensing, IEEE Transactions on, 45, 1715–1725. doi:10.1109/TGRS.2006.888103.

Schumann, G. J.-P., Neal, J. C., Mason, D. C., & Bates, P. D. (2011). The accuracy of sequential aerial photography and sar data for observing urban flood dynamics, a case study of the uk summer 2007 floods. Remote Sensing of Environment, 115, 2536–2546. URL: http://www.sciencedirect.com/science/article/pii/S0034425711001854. doi:10.1016/j.rse.2011.04.039 .

Smith, P. J., Thornhill, G. D., Dance, S. L., Lawless, A. S., Mason, D. C., & Nichols, N. K. (2013). Data assimilation for state and parameter estimation: application to morphodynamic modelling. Quarterly Journal of the Royal Meteorological Society, 139, 314–327. URL: http://dx.doi.org/10.1002/qj.1944. doi:10.1002/qj.1944 .

Thornhill, G., Mason, D., Dance, S., Lawless, A., Nichols, N., & Forbes, H. (2012). Integration of a 3d variational data assimilation scheme with a coastal area morphodynamic model of morecambe bay. Coastal Engineering, 69, 82–96. URL: http://www.sciencedirect.com/science/article/pii/S0378383912001056. doi:http://dx.doi.org/10.1016/j.coastaleng.2012.05.010 .

Vörösmarty, C., Askew, A., Grabs, W., Barry, R. G., Birkett, C., Dell, P., Goodison, B., Hall, A., Jenne, R., Kitaev, . L., Landwehr, J., Keeler, M., Leavesley, G., Schaake, J., Strzepek, K., Sundarvel, S. S., Takeuchi, K., Webster, F., & Group, T. A. H. (2001). Global water data: A newly endangered species. Eos Trans. AGU,

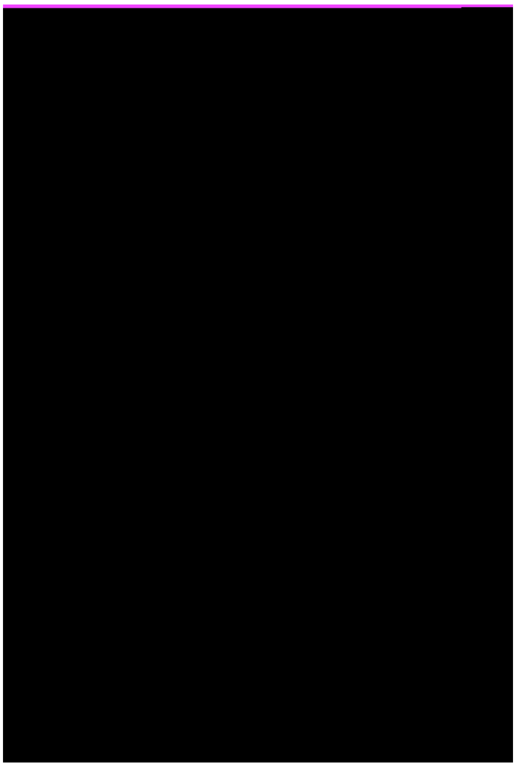

Figure 1: Flood model domain. OSGB 1936 British National Grid projection; coordinates in meters. Grey labels indicate the three larger rivers (thick black lines). The red polygon surrounds the Tewkesbury urban area. Orange labels/dots refer to the 7 in ow boundary conditions, some of them on smaller tributaries (thin black lines). The yellow line to the South indicates a free-surface boundary condition, with the label indicating the prior mean bed slope. Red labels/green dots show locations with available stage observations, just used for validation in the forecast mode. The background is the 75 m resolution DEM used for the model, obtained by upscaling the 5 m NEXTMAP British digital terrain model.

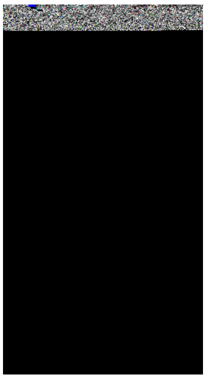

Figure 2: Flood extents (blue) for the forecast event (November 2012), overlain on SAR in ood model domain.

Figure 3: In ows into the ood domain for the forecast event, in November 2012. As a reference, blue lines are in ows as measured by standard gauges (not used as data input here). Grey lines are the 150-member forecast ensemble from the hydrologic models, used as input by the ood model. Dashed red lines are the ensemble means. Vertical dashed lines show COSMO-SkyMed overpass times.

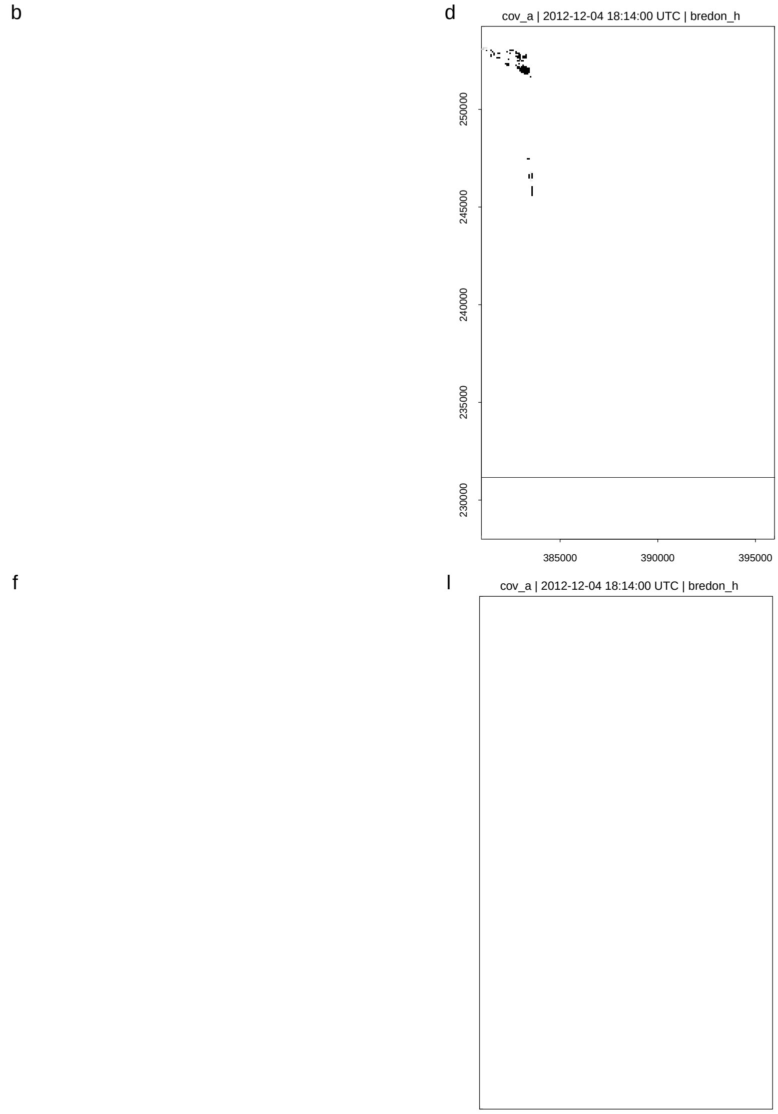

Figure 4: Updated error covariance between the state variable (water level) at Bredon and the state vector (water level elsewhere) at the last assimilation step (7th CSK overpass). Plot labels (b, d, f, and l) refer to the corresponding filters (see Table 2). The red circle indicates the location of Bredon. The set of squares, with each one centered at the corresponding observation location, is a symbolic representation of $K_{i,:}$ (being i the state vector index corresponding to water level Bredon) at the corresponding assimilation step and filter. The side length of each square is proportional to the corresponding $K_{i,j}$ value, where the biggest square in each plot relates to $\max K_{i,:}$ (e.g., 0.023 in filter [b]). The sum of the absolute Kalman gain values in the row is indicated by $\sum_{j=1}^{p}|K_{i,j}|$. Green/red squares are positive/negative gain values.

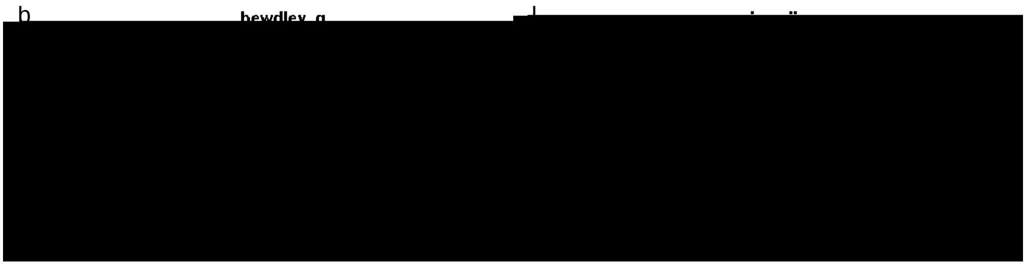

Figure 5: In ow estimation at Bewdley for lters with con guration (b) and (l), as speci ed in Table 2.

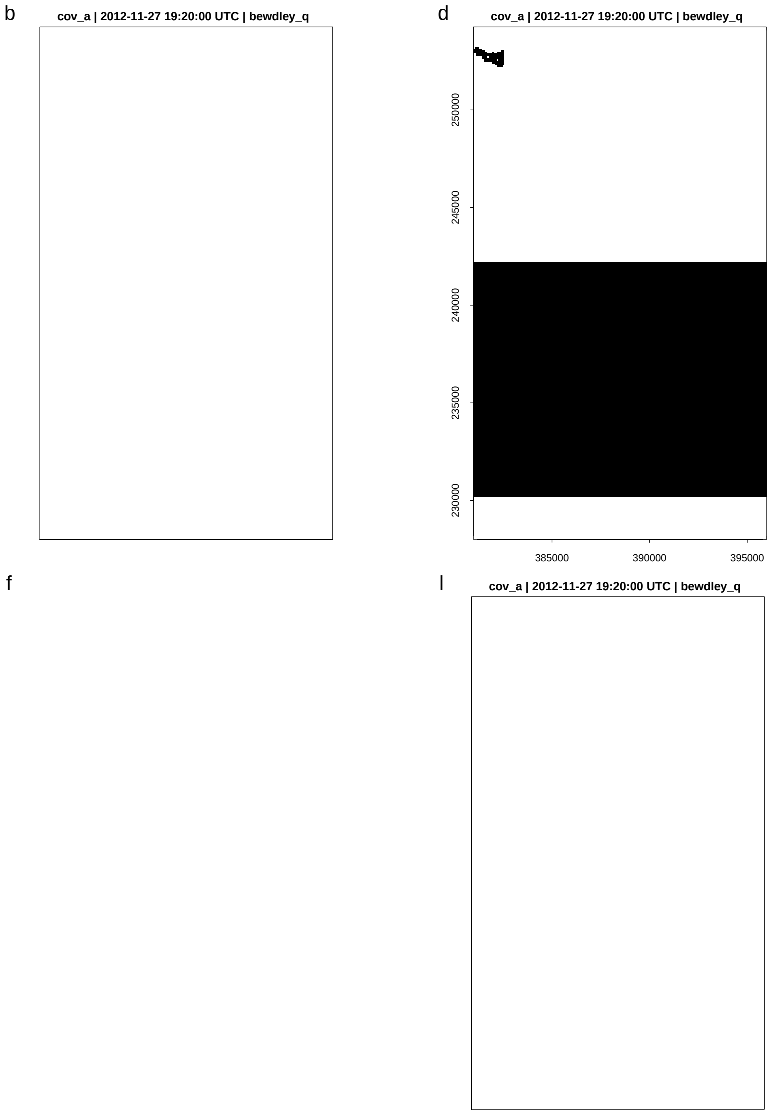

Figure 6: Updated error covariance between the inflow boundary conditions at Bewdley and the state vector (water level elsewhere) at the first assimilation step (1th CSK overpass) for the same filter than Fig. 4. Plots focus on the satellite coverage area, thus Bewdley location is not shown. Description is as Fig. 4, being the highest state vector index corresponding to inflow errors at Bewdley.

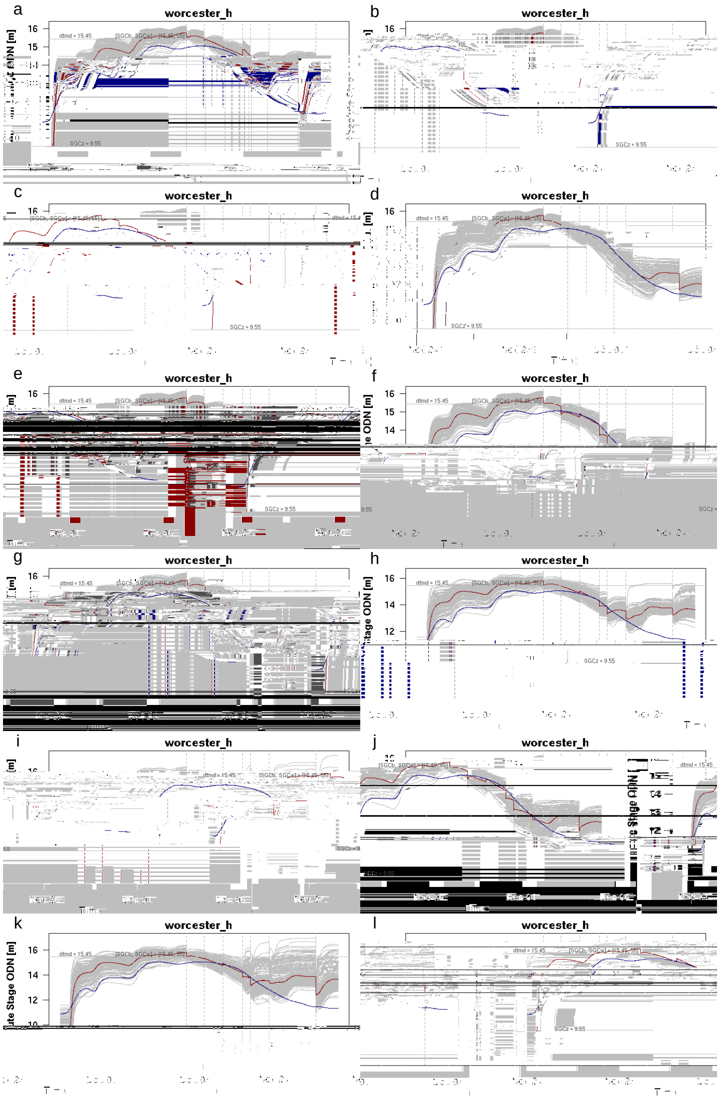

Figure 7: Water level forecast at Worcester, whose major inflows come from Bewdley (river Severn), Kidder Callows Ln Us (river Stour), and Harford Hill (river Salwarpe). Plot labels refer to the corresponding filter configurations (Table 2). For each plot, grey lines are the forecast ensemble, the red line is the mean forecast and the blue line is the gauged water level, included as a reference. Vertical dashed lines indicate the times of the CSK overpasses/assimilation. Horizontal lines indicate the bank level (labelled as “dtmd”), and the prior mean channel bottom level (labelled as “SGCz”).

Figure 8: Water level forecast at Mythe Bridge, in the Severn. Description as in Fig. 7.

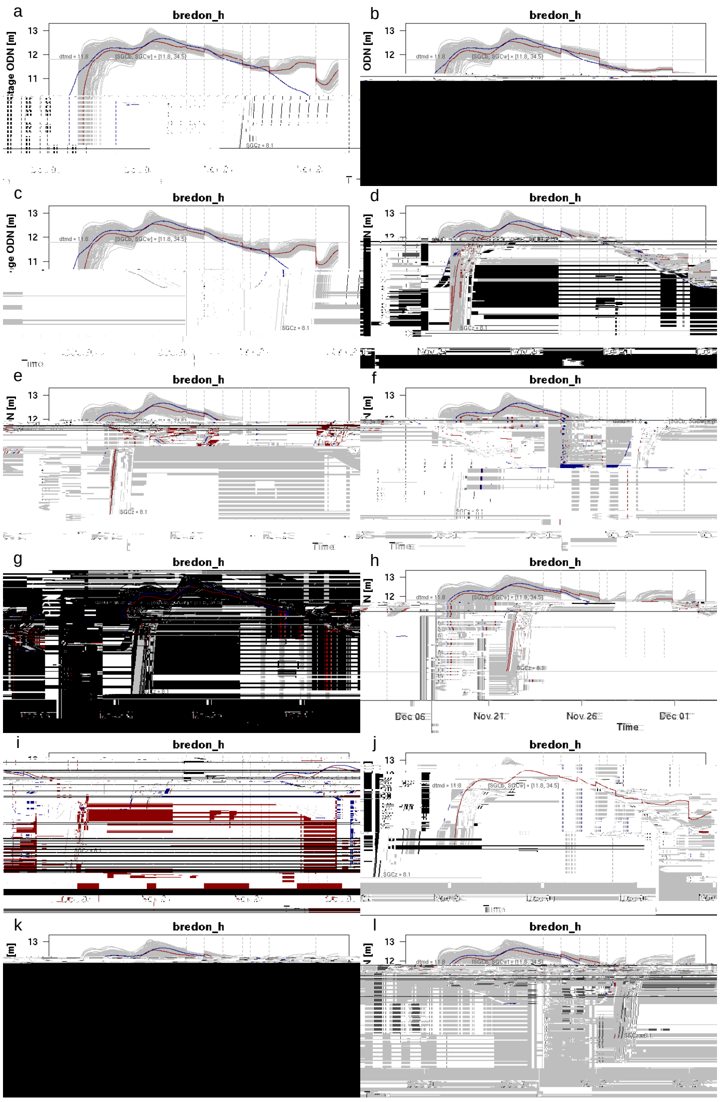

Figure 9: Water level forecast at Bredon, in the Avon. Description as in Fig. 7.

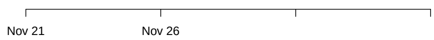

Figure 10: Evolution of the estimate of the global Manning's coe cient along the sequential assimilation steps for the three major rivers (Severn, Avon, and Teme), and lter con guration (j).

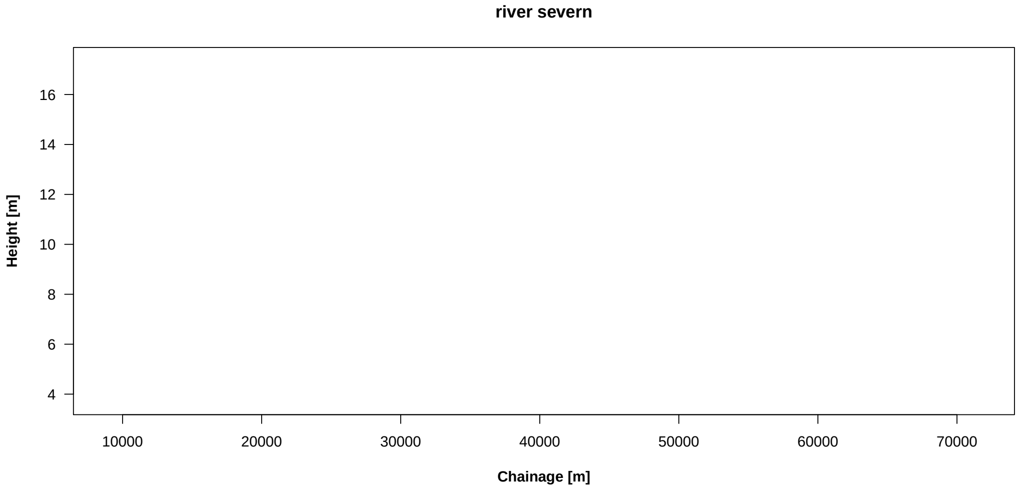

Figure 11: Evolution of the estimate of bathymetry along the sequential assimilation steps for the river Severn (top), and the Avon (bottom), for the lter con guration (k). The ticks at the bottom indicate the location of the available cross sections. The vertical dashed lines and corresponding labels indicate the location of level gauges used for water level validation.